

# Tuning MXenes Towards Their Use in Photocatalytic Water Splitting

Diego Ontiveros , Sergi Vela , Francesc Viñes\* , and Carmen Sousa 

**Finding appropriate photocatalysts for solar-driven water (H<sub>2</sub>O) splitting to generate hydrogen (H<sub>2</sub>) fuel is a challenging task, particularly when guided by conventional trial-and-error experimental methods. Here, density functional theory (DFT) is used to explore the MXenes photocatalytic properties, an emerging family of two-dimensional (2D) transition metal carbides and nitrides with chemical formula  $M_{n+1}X_nT_x$ , known to be semiconductors when having  $T_x$  terminations. More than 4,000 MXene structures have been screened, considering different compositional (M, X,  $T_x$ , and  $n$ ) and structural (stacking and termination position) factors, to find suitable MXenes with a bandgap in the visible region and band edges that align with the water-splitting half-reaction potentials. Results from bandgap analysis show how, in general, MXenes with  $n = 1$  and transition metals from group III present the most cases with bandgap and promising sizes, with C-MXenes being superior to N-MXenes. From band alignment calculations of candidate systems with a bandgap larger than 1.23 eV, the minimum required for a water-splitting process,  $Sc_2CT_2$ ,  $Y_2CT_2$  ( $T_x = Cl, Br, S$ , and  $Se$ ) and  $Y_2Cl_2$  are highlighted as adequate photocatalysts.**

## 1. Introduction

In nowadays energy landscape, the predominant reliance on conventional fossil fuels, including coal, petroleum, and natural gas, persists, despite their non-renewable nature and adverse environmental impact.<sup>[1]</sup> Nevertheless, there is a notable shift towards renewable energy sources, driven by their inexhaustible availability, independence from external factors, and lower carbon dioxide (CO<sub>2</sub>) fingerprint. The increasing preference for renewable energies is driven by their pivotal role in advancing technology and the collective effort to mitigate global warming.<sup>[2]</sup> In this context, hydrogen (H<sub>2</sub>), a clean-burning fuel, emerges as a highly promising candidate for achieving these objectives, and thus the transition to H<sub>2</sub>-based green fuels is increasingly taking place.<sup>[3]</sup> To harness H<sub>2</sub> in a sustainable manner, the focus has shifted to water splitting, employing catalysts to facilitate the cleavage of water (H<sub>2</sub>O) into H<sub>2</sub> and oxygen (O<sub>2</sub>), given the process high-energy demand. Another viable option involves the use of sunlight as an


energy vector for materials to carry out the process, acting as photocatalysts for water splitting.<sup>[4]</sup> Since experimentally, the search for adequate photoactive materials can be expensive, cumbersome, and time-consuming, the identification of suitable photocatalysts is sought to be accelerated with advanced computational screening methodologies using density functional theory (DFT).

In recent years, two-dimensional (2D) materials have emerged as a prominent topic of interest, owing to their promising physical, electrical, chemical, and optical properties.<sup>[5,6]</sup> These materials hold potential for various cutting-edge applications in fields such as energy storage,<sup>[7]</sup> gas sensing,<sup>[8]</sup> catalysis,<sup>[9]</sup> and notably, photocatalysis.<sup>[10,11]</sup> Since the initial discovery of graphene,<sup>[12]</sup> the research community has witnessed an increasing exploration of diverse 2D materials. Here we drive the attention towards MXene compounds as potential photoactive materials for water splitting.

MXenes are a fast-growing family of few-layered 2D transition metal (TM) carbides and nitrides, with  $M_{n+1}X_n$  chemical formula, where M is an early TM from groups III to VI —i.e. Sc, Y, Ti, Zr, Hf, V, Nb, Ta, Cr, Mo, and W—, X can be carbon or nitrogen, and  $n = 1-3$ .<sup>[13]</sup> The synthesis of MXenes mainly involves the selective etching of A elements from bulk layered MAX materials precursors,  $M_{n+1}AX_n$ , where A is generally a group XIII–XVI element.<sup>[14]</sup> The etching process is generally carried out using a hydrofluoric (HF) solution,<sup>[15]</sup> resulting in the functionalization of MXenes surfaces with a termination, denoted as  $T_x$ , thereby updating the chemical formula to  $M_{n+1}X_nT_x$ . While conventional HF-based synthesis commonly yields terminations such as O, F, OH, and H,<sup>[16]</sup> newer studies using synthesis methods based on molten salts have reported MXenes terminated in S, Se, Te, NH, Cl, Br, and I, and with no termination, i.e. pristine MXenes.<sup>[17,18]</sup>

Since their first discovery in 2011,<sup>[19]</sup> MXenes have been revolutionizing research across diverse fields,<sup>[20]</sup> showcasing a wide range of versatile applications. These encompass environmental uses, such as the removal of pollutant gases and CO<sub>2</sub> storage,<sup>[21,22]</sup> catalytic applications, with MXenes emerging as promising electrocatalysts for the hydrogen evolution reaction (HER) or CO<sub>2</sub> reduction,<sup>[23,24]</sup> as well as applications in energy storage, such as supercapacitors,<sup>[25]</sup> solar cells,<sup>[26]</sup> or Li-ion batteries,<sup>[27]</sup> and even biomedical applications.<sup>[28]</sup> Given their 2D structure with high surface area, unique electronic properties, and high tuneability in their composition, MXenes also show a promising future in photocatalysis.<sup>[29]</sup> There have been experimental reports of MXene nanocomposites showing excellent photocatalytic performance

D. Ontiveros, Dr. S. Vela, Prof. F. Viñes, Prof. Dr. C. Sousa  
Departament de Ciència de Materials i Química Física & Institut de Química Teòrica i Computacional (IQTCUB), Universitat de Barcelona, c/ Martí i Franquès 1-11, 08028, Barcelona, Spain  
E-mail: francesc.vines@ub.edu

 The ORCID identification number(s) for the author(s) of this article can be found under <https://doi.org/10.1002/eam2.12774>.

DOI: 10.1002/eam2.12774

for different reactions,<sup>[30–32]</sup> while theoretical studies also pose MXenes as promising materials for the photocatalytic CO<sub>2</sub> reduction<sup>[33]</sup> and water splitting.<sup>[34,35]</sup> While prior theoretical investigations have explored the use of MXenes as photoactive materials for water splitting, a majority of them focus on a few specific cases<sup>[34,36]</sup> or MXene nanocomposites.<sup>[37]</sup> The present study particularly offers an unprecedented comprehensive computational study over a wide range of MXenes, including those that have not been extensively investigated before, such as group V and VI C-MXenes, all N-MXenes, and those incorporating the novel terminations mentioned earlier. Moreover, MXenes do not necessarily have to follow the regular ABC stacking inherited from their precursor MAX phase, and some pristine and O-terminated MXenes, with  $T_x = O_2$ , have been shown to prefer an ABA stacking,<sup>[38]</sup> which influences their electronic properties.<sup>[39]</sup> Thus, here we also consider all possible structures, including the two possible stackings of the MXene and all the feasible  $T_x$  sites on the surface, often neglected in most studies.

Given the large variability in composition and structure that MXenes possess, a good starting point to identify the most promising candidates for water-splitting photocatalysis, while discarding less viable ones, is through a comprehensive computational screening of their possible configurations.<sup>[40]</sup> Here, DFT is systematically employed in MXene slab models to evaluate a wide range of factors affecting the bandgap and band alignment. The three widths,  $n = 1–3$ , both C and N as the X atom, the aforementioned groups III to VI TM, and O, F, OH, H, S, Se, Te, NH, Cl, Br, and I terminations are considered here as the possible composition for the studied MXenes. On top of that, different stackings and termination positions will also be explored for each case, reaching over 4,000 different MXene structures. For those MXenes with semiconductor properties, their adequacy to photocatalyze the water-splitting process is also evaluated by evaluating the alignment of the valence and conduction bands edges with respect to the redox potentials of the water-splitting half-reactions. Earlier works have tackled the high-throughput computational screening on MXenes for transistors and electronic devices.<sup>[41,42]</sup> However, previous studies in the photocatalysis field severely under-considered the compositional and conformational MXene space,<sup>[43,44]</sup> and sometimes using exchange-correlation DFT functionals is not suited for describing the electronic structure of semiconducting materials. Thus, to the best of our knowledge, none of these studies have specifically targeted photocatalytic properties to the extent undertaken in the present investigation.

Note that, while the bandgap size and placement of the valence and conduction bands are necessary prerequisites for photocatalytic water splitting, they alone do not encompass the entirety of the process,<sup>[45]</sup> and other aspects, including optical absorption,<sup>[46]</sup> exciton formation, carrier mobility,<sup>[47]</sup> and the actual reaction energy profile and kinetics in the excited state<sup>[48,49]</sup> can bias the full process and should be regarded in posterior studies after the present screening. Nevertheless, the photocatalytic performance of semiconductor materials possessing the right bandgap size and band alignment has been experimentally proven on well-established materials, such as rutile and anatase TiO<sub>2</sub> and ZnO,<sup>[50–52]</sup> the former explicitly computationally evaluated on rutile TiO<sub>2</sub> (110) surface.<sup>[49]</sup> Such works validate the presently used assessment approach to propose candidate MXenes as educated guesses. Additionally, this comprehensive dataset offers a valuable resource for researchers in the field, providing a standardized platform for comparison and further exploration, not only for water splitting but also for other photocatalytic processes and applications.

## 2. Results and Discussion

### 2.1. Structure

Before studying the photocatalytic properties of the whole set of MXenes considered in the present study, it is relevant to assess their different stabilities and structural parameters. Nevertheless, the large number of terminated MXenes to be considered would lead their detailed discussion on a tangent. To avoid so, a deep discussion is provided for pristine MXenes, while divergent trends are commented on for terminated ones since generally they follow similar patterns to their pristine counterparts.

Pristine MXenes were optimized at the PBE level, and the relative stability between ABC and ABA stackings was computed by their energy difference, i.e.  $\Delta E_{\text{stack}} = E_{\text{ABA}} - E_{\text{ABC}}$ , see Figure 1a. From the optimized geometries, the lattice parameter,  $a$ , and width,  $d$ , were gathered and presented in Figure 1b,c, respectively. The energy values and structural parameters for both stackings can be found in Tables S1 and S2 of the Supporting Information. Looking at the energies one first observes that, in most cases, ABC is preferred over ABA ( $\Delta E_{\text{stack}} > 0$ ). C-MXenes show higher stability for ABC stacking for all TMs except W, Mo, and Cr, which display almost degenerate stackings specially for  $n = 1$ . On the contrary, N-MXenes present lower  $\Delta E_{\text{stack}}$ , except for Y<sub>2</sub>N, Y<sub>3</sub>N<sub>2</sub>, and W <sub>$n+1$</sub> N <sub>$n$</sub>  ( $n = 1–3$ ), and generally have more cases favoring ABA stacking. This lowering in  $\Delta E_{\text{stack}}$  with respect to C-MXenes is more substantial in groups IV and V MXenes, with a decrease of 0.62, 1.74, and 2.58 eV in average for  $n = 1, 2$ , and 3, respectively, while for groups III and VI, it is more subtle. Increasing  $n$ , the patterns are similar, but the preference for a given stacking is accentuated, i.e. the magnitude of  $\Delta E_{\text{stack}}$  increases or decreases linearly with  $n$ , except for the beforementioned Cr C-MXene and V N-MXene. This variation is around 1 eV each  $n$  for group III MXenes and group V C-MXenes and somewhat stronger, 1.3 eV, for group IV C-MXenes, while for N-MXenes or the ones that prefer ABA stacking, the variation is smaller, for example, group VI N-MXenes decreasing  $\sim 0.4$  eV per  $n$ .

Regarding the lattice parameter,  $a$ , there is no significant variation observed when increasing the number of layers of the MXene,  $n$  (cf. Figure 1b). All exhibit a similar trend, wherein the first 3d TM of each group shows a lower value for  $a$ . Subsequently, there is a notable increase of approximately 0.2 Å in the 4d TM, while the 5d TM remains roughly constant. The sole exceptions for this trend are group VI N-MXenes with ABC stacking, which exhibit Mo and W cases with unusually lower lattice constants than Cr. Regarding the X atom, C-MXenes present slightly larger cell parameters than N-MXenes, apart from the ABC Nb and Cr MXenes with  $n = 1$  and 3, with the decrease in  $a$  being normally less than 6%, except Mo<sub>3</sub>X<sub>2</sub>, Mo<sub>4</sub>X<sub>3</sub>, W<sub>3</sub>X<sub>2</sub>, and W<sub>4</sub>X<sub>3</sub> cases with ABC configuration, which show larger variations. Similarly, ABC stacking presents higher lattice parameters than ABA, around 0.1 Å on average, with the exception of Mo and W N-MXenes.

As per the MXene width,  $d$ , similar trends are gathered (cf. Figure 1c). However, there is an inversion in the difference between stackings, with ABA structures now exhibiting higher width values compared to ABC structures. This inversion is also noticeable comparing C- and N-MXenes, particularly for ABA-stacked N-MXenes, where they display higher widths than C-MXenes. Here we can see again the untrendy behavior of Mo and W ABC N-MXenes, showing larger width values than expected. These larger widths and smaller cell parameters for ABA stacking can be explained in terms of steric repulsions between the M layers. For ABA, the repulsions are only along the vacuum

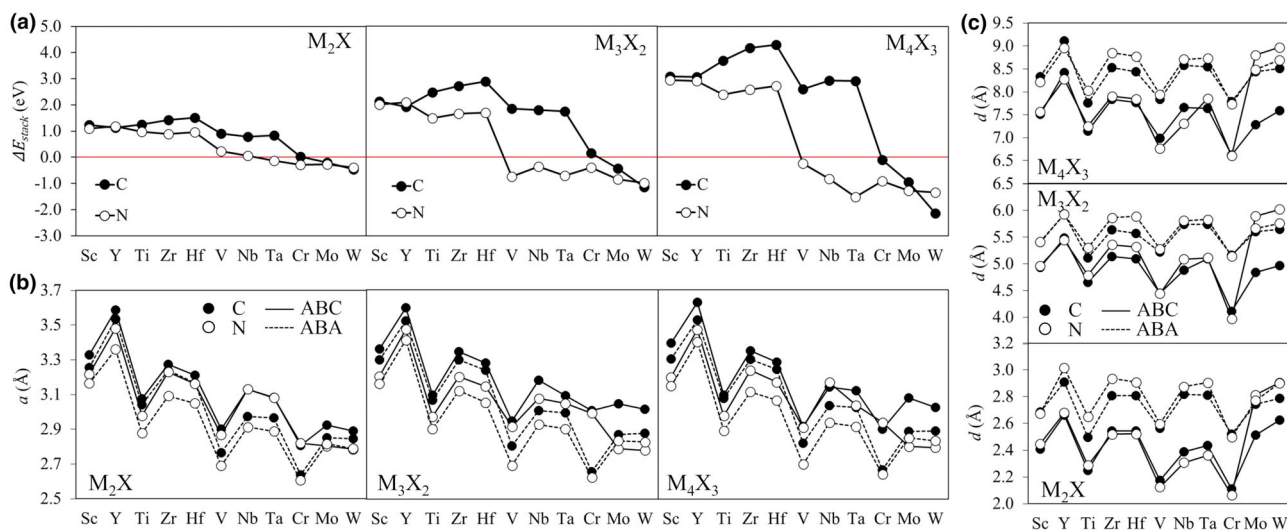


**Figure 1.** a) Energy difference between ABC and ABA stacking,  $\Delta E_{\text{stack}}$ , in eV, for the studied pristine MXenes, where the points above or below zero (red line) indicate a preference for the ABC or ABA structure, respectively. b) Lattice parameter,  $a$ , in Å, and c) width,  $d$ , in Å for the  $n = 1-3$  pristine MXenes. In all cases, the black and white filled dots indicate C and N MXenes, respectively, while straight and dashed lines indicate ABC and ABA stacking, respectively.

direction, leading to larger widths, while for ABC there exists some lateral component that makes the lattice parameter larger.

It is well known that adding a termination brings a positive net stabilization to the MXene. The formation energy has been calculated for various terminated MXenes,<sup>[51,53]</sup> leading to the conclusion that terminated MXenes are energetically stable. Thus, in the following, we will focus on the stability between the different conformations, assessed by calculating the relative energy with respect to the ABC  $H_M$  structure,  $\Delta E$ . In Figure 2, one finds the relative energies in the case of Cl-terminated MXenes as a representative example, while the relative energies for the other cases are found in Figure S2 of the Supporting Information. In general, as in the pristine MXenes, there is a preference for ABC stacking, especially for groups III and IV MXenes and group V C-MXenes, while N-MXenes tend to present more ABA cases, especially

for group V and VI transition metals. There are some exceptions that all favor the ABC  $H_M$  geometry for all the metals, for example, the  $M_2\text{CCl}_2$ ,  $M_2\text{CBr}_2$ , and  $M_2\text{XTe}_2$  systems. When increasing  $n$ , one normally sees a linear increase in the variation of the  $\Delta E$ , reinforcing the stacking preference, as seen for pristine MXenes, and also maintaining the same hollow preference. The preferred termination position depends significantly on the TM, X, and  $T_x$  termination, but in most cases seems to follow that, for each stacking, the most stable hollow site is  $H_M$  for ABC or H for ABA, then followed by  $H_{MX}$ , and finally  $H_X$ , except for some group V and VI systems, where the order is inverted. It is important to notice that S- and Se-terminated group III C-MXenes have a clear preference for  $H_{MX}$  instead of the usual  $H_M$ , which also happens when O-terminated,<sup>[53]</sup> showcasing how atomic terminations of the same group may lead to similar stability and properties.

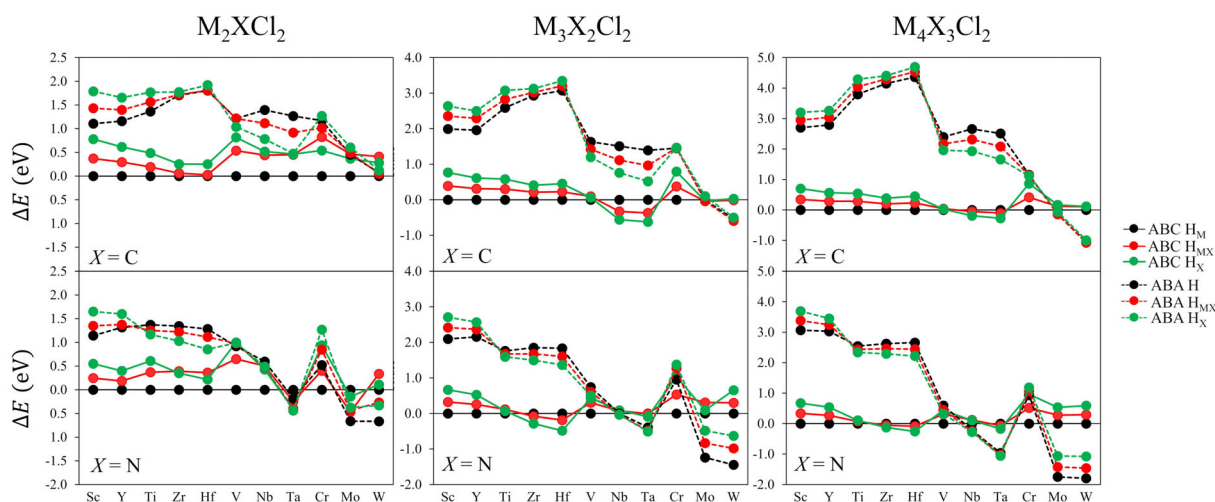


**Figure 2.** Relative energies,  $\Delta E$ , in eV, of the six configurations of Cl-terminated MXenes for the three different  $n$ , with respect to the ABC  $H_M$  structure.

Regarding the geometry of terminated MXenes, similar patterns to pristine MXenes are gathered, see the representative Br-terminated cases in Figure S3 of the Supporting Information, maintaining the untrendy behavior of Mo and W ABC N-MXenes in all cases. The  $a$  values are in the same range in all terminations except when  $T_x = S, Se, Te, I$ , where their large volume slightly deforms the cell, leading to larger cell parameters and widths. The variations in  $a$  between the termination position are almost negligible, while for the widths, generally, one sees  $H_X$  structures presenting larger  $d$  values, given the more direct  $T_x$ -X repulsions, while  $H_M$  or H show smaller  $d$ .

## 2.2. Bandgap

The photoactive properties of the studied MXenes were firstly assessed by gaining the density of states (DOS) and searching which systems present an adequate bandgap, larger than 1.23 eV (the minimum demanded for the water-splitting process), ideally landing on the visible region (1.8–3.1 eV) to profit from maximal solar light intensity. The DOS has been calculated both at PBE and PBE0 levels. However, as aforementioned, since hybrid functionals are known to better describe the bandgap of semiconductor compounds,<sup>[54]</sup> the electronic properties will be described based only on the PBE0 values. Consistent with previous studies,<sup>[55,56]</sup> pristine MXenes exhibit metallic properties similar to their precursor MAX phases. Therefore, they will not be the primary focus of discussion in this context.

On the other hand, when terminated, some MXenes are known to become semiconductors, for example, group III and IV MXenes terminated with O.<sup>[35,53]</sup> Even though terminated MXenes have an energetically preferred structure among the six configurations previously investigated, it is crucial to evaluate the impact of stacking and hollow position on the electronic properties of MXenes. Additionally, it is worth considering that certain structures display minimal differences in energy between different hollow positions and stacking, such as  $Y_3C_2Se_2$ ,  $Ti_3N_2Cl_2$ , or  $V_2XS_2$  (see Figure 2 and Figure S2 of

the Supporting Information), making it convenient their further study, assuming that different phases could coexist.

From the 4356 studied terminated MXenes (having added the 132 corresponding to the  $n=1$  O-terminated MXenes of previous studies<sup>[35]</sup>), only 945 presented a bandgap, and from those, 243 displayed a bandgap larger than 1.23 eV. In Figure 3, the PBE0 bandgap values for the most representative cases are presented, and in Figure S4 of the Supporting Information six more cases can be found. The full set of PBE0 values for MXenes with a bandgap is available in Table S3 of the Supporting Information. First, the structural (stacking and termination hollow position) and compositional ( $n$ ,  $X$ ,  $M$ , and  $T_x$ ) factors were examined regarding the percentage of cases that exhibit bandgap on the semiconducting MXene pool, with the results gathered in Figure 4. In terms of  $n$ , we can see how most semiconductors are within  $M_2XT_2$  ( $n=1$ ) MXenes, and the number quickly decays for larger  $n$ . Increasing  $n$  leads to more M-X layers, growing the bulk of pristine MXene, which is known for its metallic properties. This recurring pattern can be observed not only in the bandgap and conducting properties but also in a broader context, for instance, in the aforementioned increased separation of stacking energies. It is evident that as the value of  $n$  increases, and the quantity of bulk material expands, the properties of the bulk are enhanced while the impact of terminations is diminished.

Approximately 70% of the  $E_g > 0$  cases consisted of C-MXenes, whereas N-MXenes accounted for a much lower percentage of 30%. N-MXenes not only have a reduced number of semiconducting cases showing a sizeable bandgap, but in most cases, as depicted in Figure 3, the corresponding values are generally smaller as well,  $\sim 0.5$  eV on average. To comprehend this behavior, Figure S5 of the Supporting Information, compares the band structure and projected DOS of  $Y_2CH_2$  vs  $Y_2NH_2$ , revealing when C-MXenes exhibit a bandgap, as in the example, the corresponding N-MXenes often show a very similar band structure, but due to the additional electrons introduced by N atoms, the conduction band becomes partially filled, resulting in a metallic behavior. The few exceptions concern group III  $M_3X_2O_2$ ,  $M_3X_2(NH)_2$ , and  $M_4X_3(NH)_2$  structures, which are metallic when  $X=C$ , in accordance

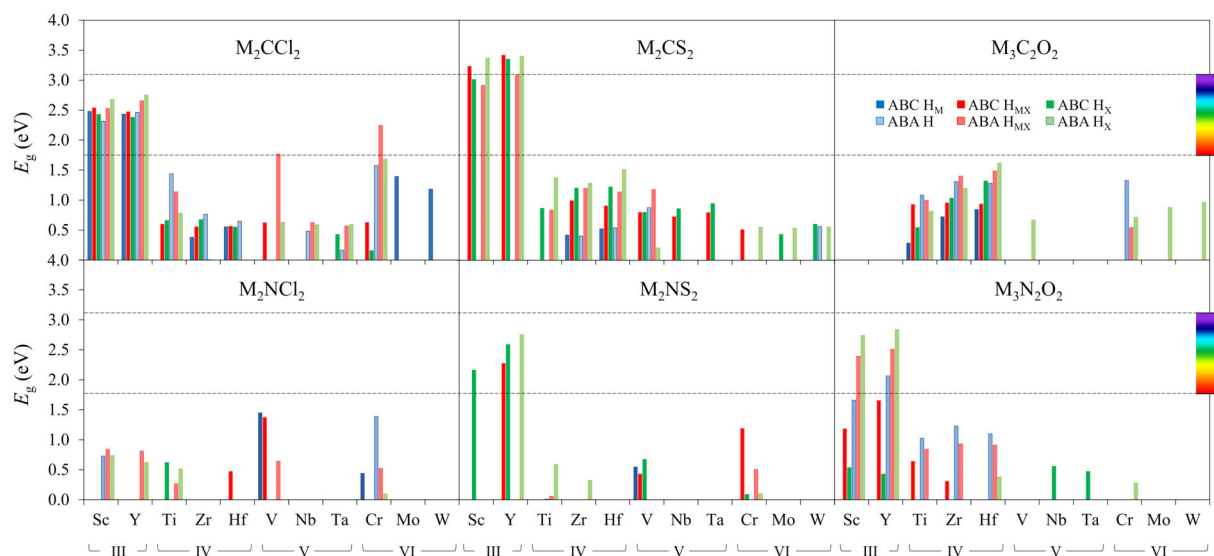


**Figure 3.** Calculated bandgap,  $E_g$ , in eV, at PBE0 level, for the six different geometries of the  $M_2XCl_2$ ,  $M_2XS_2$ , and  $M_3X_2O_2$  selected MXenes, considered as representative. In each plot, the range of the visible spectrum is displayed, from 1.8 to 3.1 eV.



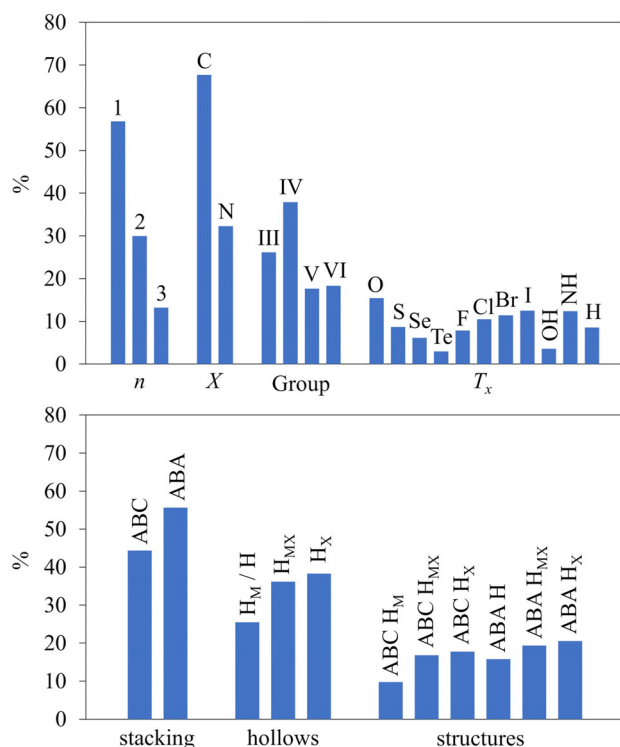


**Figure 4.** Percentage of cases with bandgap for different compositional ( $n$ ,  $X$ ,  $M$ ,  $T_x$ ) and structural (stacking and hollows) factors.

with previous studies,<sup>[57]</sup> but display a bandgap in most of the  $X=N$  configurations. When considering the TM elements, group III and IV MXenes exhibit a significantly greater number of cases with bandgap compared to the other metal groups. Moreover, these MXenes also present larger bandgap values on average. Specially group III, typically landing within the visible region, or even higher, emerging as promising candidates for photocatalytic applications. The TM plays an important role in the bandgap appearance; the PDOS shown in Figure S5, Supporting Information, serves as a general example of how the valence (VB) conduction (CB) bands are distributed. Below the Fermi level,  $E_F$ , two VBs always appear, with main contributions from  $X$  and  $T$  atoms, at higher and lower energies, respectively, while the CB is mainly contributed by the TM atom. Although the reason why group III cases exhibit higher bandgap values is not entirely clear, one possible general explanation could be that when combining Sc and Y with an electronegative halide or chalcogenide termination, the resulting combination forms a more ionic material with a more localized charge. This is in contrast to groups V or VI TM, where being less electropositive results in more covalent interactions and a lower probability of a bandgap.

Regarding terminations, the quantity of semiconductor systems and their bandgap may fluctuate based on the chemical nature of the termination. For instance, halogen terminations present a considerable number of cases, but in the case of Te- and OH-terminated MXenes, almost all systems are metallic. Generally, the majority of those semiconducting cases are group III and IV metals, presenting larger bandgap values than the rest, which is a common pattern for all  $n=1$  MXenes. Between terminations, group III MXenes present larger bandgap values for chalcogen terminations, followed by halogen-terminated MXenes, H, NH, and finally OH with the lowest values on average. Among the

examined systems, the termination leading to the highest number of semiconductor structures is O, mainly with  $n=1$  but also including a few cases with  $n=2$ . One thing to be noted is that within terminations from the same group, when increasing the period, halogen terminations increase the number of cases while for chalcogens this number decreases drastically, although the average value of semiconducting systems of the former is generally lower than the latter.

To rationalize the effect of the termination on the electronic properties, it is important to note that, in pristine MXenes, the Fermi level lands on the  $d$  orbital band from the TM, as illustrated in Figure S6 of the Supporting Information, with the  $p-X$  bands situated lower in energy, often separated by a tiny gap. As mentioned before, when adding the termination, its  $p$  orbital bands appear at lower energies than  $E_F$ , and usually below the  $p-X$  band. These new  $p-T$  bands shift downwards the Fermi level, and depending on the surface termination and its interaction, this shift can land on the mentioned gap between the  $X$  and TM bands. This phenomenon has been demonstrated and further explored in  $Ti_2C$  and  $Ti_3C_2$  MXenes.<sup>[53,58]</sup>

Semiconducting properties are more prominent in ABA (56%) stacked MXenes compared to ABC (44%) stacking, but there is no clear pattern determining when this occurs. For instance, in certain cases like  $Sc_2NS_2$   $H_X$  or  $Y_2NS_2$   $H_{MX}$ , ABC stacking exhibits a large bandgap while ABA stacking shows metallic behavior, and vice versa, as demonstrated in group III  $M_2NH_2$ . However, on average, ABA structures tend to have slightly larger bandgap values than their corresponding ABC stacking counterparts, with an increase of approximately 0.2 eV. The larger number and slightly higher values of bandgap in ABA cases may be attributed to less interaction between adjacent atoms between layers, which leads to less dispersed valence and conduction bands, slightly increasing the bandgap. This can be seen in the band structure comparison of  $Sc_2CF_2$  with F in the  $H_X$  position, see Figure S5 of the Supporting Information, where the conduction band is more dispersed for the ABC stacking, slightly reducing the bandgap.

As far as the termination hollow site is concerned,  $H_X$  is the most common position for systems with a bandgap in both stackings. Likewise, a consistent trend is observed where  $H_M$  or H have fewer semiconductor systems, followed by  $H_{MX}$ , and then  $H_X$ . Once again, we observe a recurring trend, also evident in the relative energies of the different termination sites and MXene widths. The values for  $H_{MX}$  structures fall between those of  $H_M$  (or H) and  $H_X$ , not surprisingly, since  $H_{MX}$  structures have one surface with  $T_x$  in  $H_M/H$  and the other with  $H_X$ . This dual composition appears to be reflected in the electronic and structural properties, resulting in values that are a combination of both  $H_M/H$  and  $H_X$ , evidenced in the band structures of the  $S_2CF_2$  example shown in Figure S5 of the Supporting Information. Concerning the bandgap values, once again, there is no definitive leader in terms of the highest values. In certain cases, such as group III  $M_3N_2O_2$  and  $M_2C(OH)_2$ ,  $H_X$  typically exhibits larger bandgaps, while in other cases, like  $M_2CH_2$ ,  $H_M$  shows higher values.

### 2.3. Band Alignment

From the semiconductor systems discussed before, the ones with a bandgap larger than 1.23 eV, the minimum demanded for the water-splitting process, were selected to calculate their band alignment with respect to the water-splitting half-reactions, see Figure 5. Before delving into the topic, it is important to acknowledge that for a semiconductor material to serve as an effective solar-light-harvesting

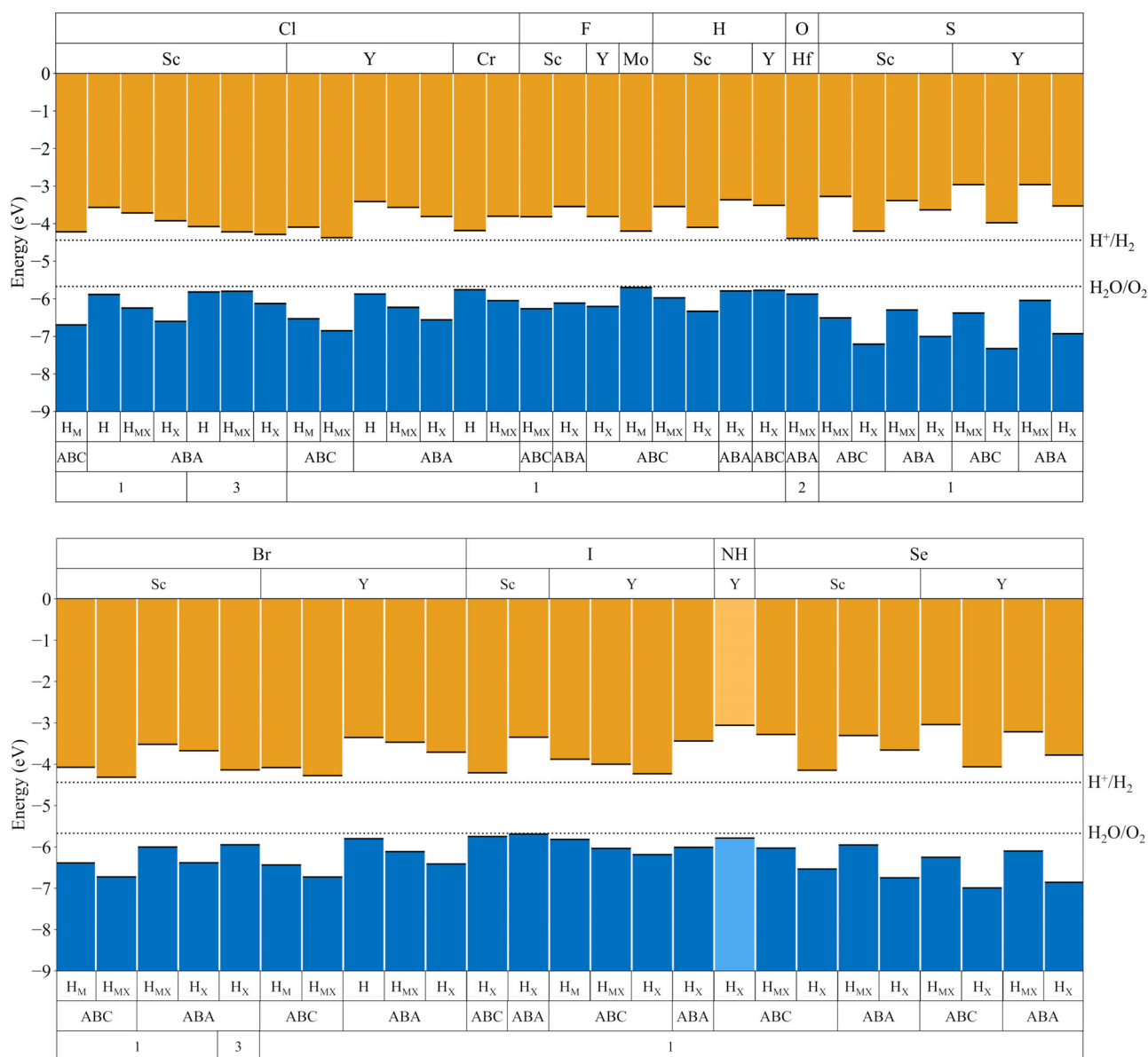


**Figure 5.** Band alignment diagrams with respect to the  $\text{H}^+/\text{H}_2$  and  $\text{H}_2\text{O}/\text{O}_2$  potential energy levels, represented as the dotted lines, for the suitable cases. The blue and orange bars indicate the VB and CB, respectively. Darker and lighter colors represent C- and N-MXenes, respectively.

photocatalyst, it must possess a bandgap that falls within the visible spectrum range. Additionally, the band edges, namely the valence band maximum (VBM) and the conduction band minimum (CBM), should surpass the potentials of the redox half-reactions. In the specific context of photocatalytic water splitting, the reduction ( $\text{H}^+/\text{H}_2$ ) and oxidation ( $\text{H}_2\text{O}/\text{O}_2$ ) potentials are  $-4.44$  and  $-5.67$  eV, respectively.<sup>[59]</sup> The VBM and CBM are calculated from the Fermi level,  $E_F$ , and the bandgap,  $E_g$ , but need to be corrected with the reference vacuum potential,  $V_v$ :

$$E_{\text{VBM}} = E_F - V_v E_{\text{CBM}} = E_{\text{VBM}} + E_g \quad (1)$$

which indicates the electrostatic potential in the vacuum region of the slab model, extracted from the local potential plot along the

vacuum direction perpendicular to the MXene surface. For the  $\text{H}_{\text{MX}}$  structures, regarded as Janus materials, with different properties on each of the two surfaces, the vacuum potential is considered the mean between both surfaces endings.

Figure 5 displays all structures that present a suitable band alignment, while Figure S7 of the Supporting Information, are presented the ones where the band edges do not align with the half-reaction potentials, but still have  $E_g > 1.23$  eV. First, it is evident that almost all the resulting suitable cases are C-MXenes, as N-MXenes exhibited very few cases with suitable bandgaps. Taking a closer look at the ABA  $\text{Sc}_2\text{CCl}_2$  and  $\text{Y}_2\text{CCl}_2$  MXenes, we can observe the previously mentioned trend where  $\text{H}_{\text{MX}}$  structures consistently exhibit average values between  $\text{H}_\text{M}/\text{H}$  and  $\text{H}_\text{X}$ . Specifically, we often observe that H has higher VBM

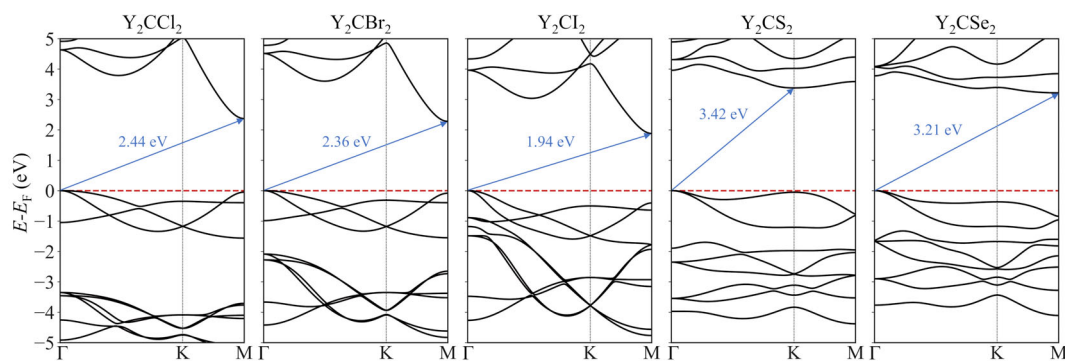


**Figure 6.** Band structure diagrams for the most stable structures of  $\text{Y}_2\text{CCl}_2$ ,  $\text{Y}_2\text{CBr}_2$ ,  $\text{Y}_2\text{CI}_2$ ,  $\text{Y}_2\text{CS}_2$ , and  $\text{Y}_2\text{CSe}_2$ , the most suitable  $M = \text{Y}$  cases found for water-splitting photocatalysis. The bandgap is marked with the blue arrow, with the value also in blue. The energies are corrected with the Fermi level.

and CBM, while  $\text{H}_\text{X}$  tends to have lower ones, with  $\text{H}_{\text{MX}}$  structures typically falling in between these values. Se-, Cl-, and S-terminated MXenes are the ones that have a higher ratio of correct band alignment vs non-adequate, 57%, 54%, and 42%, respectively, while Te- and OH-terminated MXenes do not present any suitable case. From the alignments reported in Figure S7 of the Supporting Information, one can see how, when  $\text{T}_\text{X} = \text{OH}$ , the VBM appears at unusually high values, and the band edges are way off the water-splitting half-reaction potentials. OH-terminated MXenes are known as ultra-low workfunction materials due to their surface dipole moment.<sup>[60]</sup> The workfunction,  $\phi$ , is defined as the energy required to extract an electron from the  $E_\text{F}$  and place it in the vacuum region, and is calculated as  $V_\text{V} - E_\text{F}$ , which actually is just the negative of the VBM energy, i.e.  $E_\text{VBM} = -\phi$ , hence the origin of this unusual behavior.

As mentioned in the preceding section, MXenes exhibit an energetically favored structure among the six potential configurations. Consequently, the ideal scenario from the investigated configurations would be the one that demonstrates optimal band alignment and represents the most stable structure for the respective MXene. These criteria are fulfilled by  $\text{Sc}_2\text{CCl}_2$ ,  $\text{Y}_2\text{CCl}_2$ ,  $\text{Sc}_2\text{CBr}_2$ ,  $\text{Y}_2\text{CBr}_2$ ,  $\text{Sc}_2\text{CS}_2$ ,  $\text{Y}_2\text{CS}_2$ ,  $\text{Sc}_2\text{CSe}_2$ ,  $\text{Y}_2\text{CSe}_2$ , and  $\text{Y}_2\text{CI}_2$  MXenes, that present ABC  $\text{H}_{\text{MX}}$ , when halide-terminated, and ABC  $\text{H}_{\text{MX}}$ , when chalcogen-terminated, as the most stable structures. From previous studies,  $\text{Zr}_2\text{CO}_2$  has also been found to present adequate band alignment and structure.<sup>[34,35]</sup> Some of the Sc- and Y-based MXenes, such as  $\text{Sc}_2\text{CCl}_2$  and  $\text{Y}_2\text{CCl}_2$ , have been subject to detailed examination in prior studies,<sup>[61–63]</sup> and present favorable optical absorptions on the visible range, as well as high and anisotropic charge carrier mobilities. These findings further underscore the promising characteristics of MXenes in photocatalysis, including those identified as optimal in our current study.

Most of these promising MXenes are derived from Group III transition metals, for which the synthesis is somewhat lagging compared to other groups. However, noteworthy progress has been made; for instance,  $\text{Sc}_2\text{CO}_2$  MXene was successfully synthesized using magnetron sputtering,<sup>[64]</sup> and other Sc-containing MXenes have been already obtained.<sup>[65]</sup> Additionally, MAX phases containing Sc and Y exist and are actively being synthesized.<sup>[66,67]</sup> Therefore, these materials are in closer reach, and the current results highlight them as promising candidates for water-splitting photocatalysis.

To investigate the dynamical stability of the resulting optimal MXenes, we computed their phonon spectra, see Figure S8 of the Supporting Information. None of the phonon modes exhibited major

negative frequencies, indicating the overall stability of the materials, consistent with the phonon calculations reported in other references for Sc- and Y-based systems,<sup>[63,68]</sup> while the small imaginary frequencies below  $30 \text{ cm}^{-1}$  near  $\Gamma$  point observed for S- and Se-terminated MXenes can be safely attributed to numerical noise owing to the vacuum region or the employed  $\mathbf{k}$ -point mesh.<sup>[40,69]</sup> To study more deeply these systems, in Figures 6 and 7, the band structures and

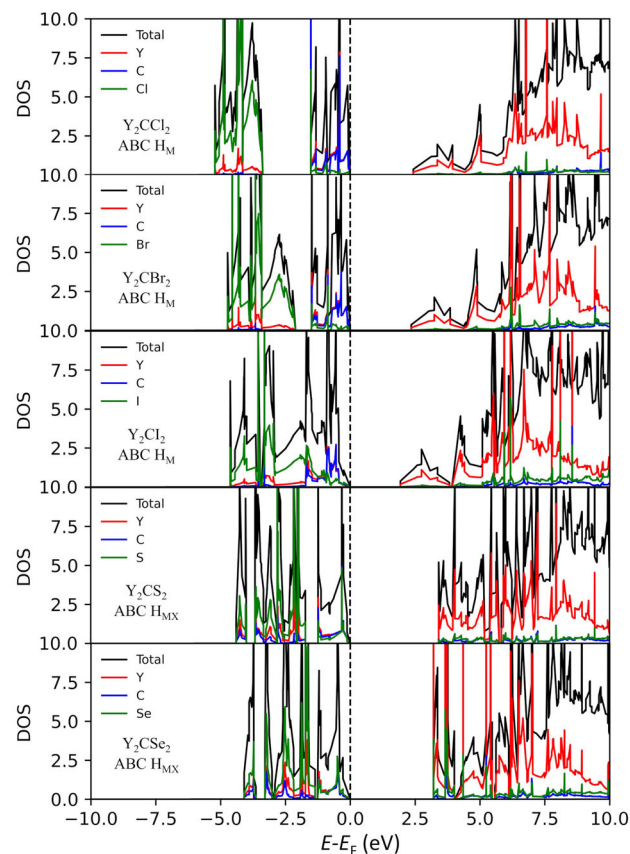


**Figure 7.** Total and atom-projected DOS for the Y-MXene promising cases. The energies are corrected with the Fermi level,  $E_\text{F}$ , marked as the dashed black line.

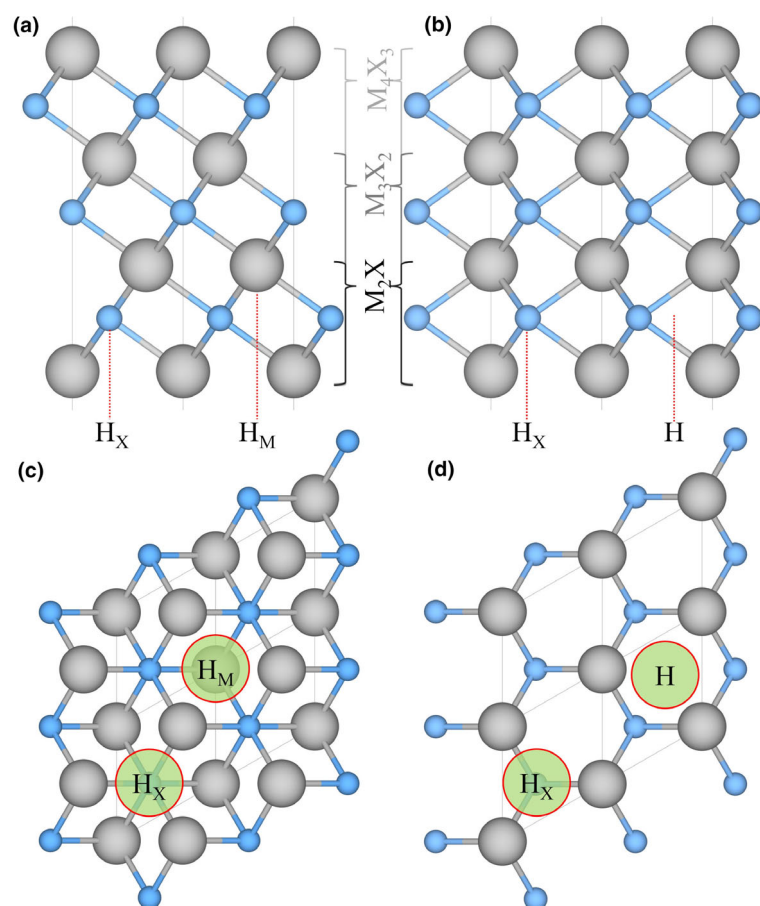


**Figure 8.** Side view of the a) ABC and b) ABA stackings for pristine MXenes, including top views of the c) ABC and d) ABA stacking MXene with  $n = 1$ . Gray and blue spheres represent the metal, M, and X atoms (C or N), respectively. The red dotted lines in a) and b) and the green circles in c) and d) mark high symmetry sites for possible termination placement —H for hollow,  $H_M$  for metal hollow, and  $H_X$  for C/N hollow. In gray the unit cell is indicated.

projected DOS are represented, respectively, for the Y-MXene promising cases, while the  $M = \text{Sc}$  are displayed in Figures S9 and S10, Supporting Information. Inspecting the DOS, one can observe how the VB is made primarily of TM and C states (in the case of halide-terminated) and has contributions of all the components when S- or Se-terminated, while the CB is dominated by the  $d$  orbitals of the TM. The band structure provides valuable insight into the bandgap characteristics for all promising cases. When  $T_x = \text{Cl, Br, I, or Se}$ , the bandgap extends from the  $\Gamma$  to the  $M$  point, whereas in S-terminated cases, the bandgap spans from the  $\Gamma$  point to the  $K$  point (or near the  $K$  point for the  $\text{Sc}_2\text{CS}_2$  system). This characteristic highlights the indirect nature of the bandgap, which is advantageous for photoactive materials in terms of promoting efficient photocatalytic reactions. In an indirect bandgap material, when an electron is excited, it requires a change in momentum to return to the ground state, resulting in the electron spending additional time in the excited state, where the photocatalytic reaction occurs.<sup>[70]</sup>

To validate the PBE0 estimates, we compared the HSE06 and GW bandgaps for the promising cases identified during the screening process in Table S4 of the Supporting Information. It is observed that the

PBE0 values are closer to those obtained via the GW approach, considered as the reference, with slight deviations of 0.13 eV on average, and consistent with previous comparative studies.<sup>[71]</sup> On the other hand, HSE06 yields systematically smaller bandgaps, which differ by 0.78 eV from the GW reference values. Thus, PBE0 estimates are found to be a suited approach for MXene semiconductor cases, validating both the findings and the methodology employed in this study.

### 3. Conclusions

In this work, the photoactive properties of a wide range of MXene compounds ( $M = \text{Sc, Y, Ti, Zr, Hf, V, Nb, Ta, Cr, Mo, and W}$ ,  $X = \text{C and N}$ ,  $n = 1-3$ , and  $T = \text{O, F, H, OH, S, Se, Te, NH, Cl, Br, and I}$ ) have been investigated with slab models and DFT calculations at PBE and PBE0 level. An exhaustive screening of these compositions, considering also different stackings and termination positions, has been carried out to search for systems with a bandgap greater than 1.23 eV, ideally landing on the visible spectra. Results showed that the cases displaying the most promising semiconductor properties were group III MXenes with  $n = 1$ , which presented a wide bandgap for almost all terminations and structures. Close in second place are group IV MXenes, which also present quite a few cases with bandgap, but the values were normally not in the visible range. Also, we gathered how C-MXenes showed much more bandgap cases with higher values than N-MXenes, which generally induce metallic behavior due to the extra electrons of the N atom. In general, as  $n$  increases, the bulk pristine material becomes more prominent, leading to enhanced pristine properties that are less influenced by the effects of the termination. This trend is particularly evident, on one hand, in the analysis of the bandgap, where the majority of cases with  $n = 2$  and 3 exhibit metallic properties, and, on the other hand, in the relative energies, where the stacking preference is reinforced as  $n$  grows. In terms

of the stacking stabilities, group III and IV MXenes usually prefer ABC stacking while group V and VI tend to favor ABA stacking, with generally  $H_M$  (H) being the most favorable hollow position for ABC (ABA) stacking.

After inspecting the MXenes structures with  $E_g > 1.23$  eV through band alignment calculations, 56 structures were gathered with a correct band alignment; 65 when including the previously reported O-terminated  $n = 1$  cases.<sup>[35]</sup> Nonetheless, since six structures are considered for each terminated MXene, the ideal cases would be the ones that also are the most stable structure. This is accomplished for the  $\text{Sc}_2\text{CT}_2$ ,  $\text{Y}_2\text{CT}_2$  ( $T = \text{Cl, Br, S, Se}$ ), and  $\text{Y}_2\text{Cl}_2$  MXenes, with an indirect bandgap in the visible region (or slightly higher for the S-terminated), which poses them as promising photocatalysts for the water-splitting process. Based on the current results, it is noteworthy that, for the synthesis of MXenes for photoactive applications, a molten salt approach<sup>[17]</sup> is highly recommended over the conventional use of hydrofluoric acid. The molten salt approach appears to yield more favorable terminations, particularly minimizing the presence of OH terminations, which are quite detrimental in the band alignment, thus jeopardizing the potential suitability of MXenes for photoactive applications.



In the present work, we underlined the photoactive properties of terminated MXene compounds and their structures in the generation of green  $H_2$  from the water-splitting process. Since the studied terminations have presented promising results, it opens the door to expanding the screening with new terminations or even combining various termination groups and TM. Previous studies already highlight the optical and electronic properties of some of the promising MXenes,<sup>[61–63]</sup> and yet further studies on optical absorption, exciton formation, carrier mobility, and reactivity on the excited state need to be carried out to better assess their photocatalytic efficiency, ideally including electronic structure analysis in terms of charge density difference (CDD) plots, or crystal orbital Hamiltonian population (COHP) as done in electrocatalytic studies.<sup>[9,72]</sup>

## 4. Computational Details

For the structural models, we focused on  $n = 1–3$  MXenes, with the chemical formula  $M_{n+1}X_n$ , when pristine, and  $M_{n+1}X_nT_x$  when terminated. Such were studied for  $M = Sc, Y, Ti, Zr, Hf, V, Nb, Ta, Cr, Mo, or W$  (group III–VI early TM), while considering both carbon (C) and nitrogen (N) as the X atom, and O, F, OH, H, S, Se, Te, NH, Cl, Br, or I as the  $T_x$  termination. Since the O-terminated with  $n = 1$  systems have previously been extensively studied,<sup>[34,35]</sup> here we studied  $n = 2, 3$  structures, while all O-terminated MXenes are included in the posterior bandgap analysis.

Pristine MXene structures consist of M and X atom intercalated close-packed layers. Two possible stackings arise for such systems; ABC stacking, see Figure 8a, with the M layers in two different relative positions, or ABA stacking, see Figure 8b, with the M layers in the same relative position along the vacuum direction. The lattice parameters and layer width employed have been optimized by DFT and the results are in line with previous DFT studies.<sup>[38,73,74]</sup> The terminated MXenes are initially built by adding the  $T_x$  atoms to the optimized pristine MXene structures, sampling different surface hollow sites, see Figure 8. Hence, various situations have been explored: the metal hollow in ABC stacking,  $H_M$ , located above an underlying metal atom, the simple hollow in ABA stacking, H, placed with no atoms underneath, the carbon or nitrogen hollows,  $H_X$ , with an underlying X atom for both stackings, and a mixture of  $H_M$  (H) and  $H_X$  on opposite MXene surfaces for ABC (ABA) stacking — $H_{MX}$ . By combining stacking and hollow sites, each terminated MXene has six possible structures, see Figure S1, Supporting Information. This site notation will be used in the upcoming discussion.

The DFT<sup>[75,76]</sup> results presented in this work were obtained using the Vienna ab initio simulation package (VASP).<sup>[77]</sup> Spin-polarized calculations were carried out using the Perdew–Burke–Ernzerhof (PBE)<sup>[78]</sup> exchange–correlation functional within the generalized gradient approximation (GGA),<sup>[79]</sup> with additional calculations applying the PBE0 hybrid functional for a more reliable bandgap estimation.<sup>[54,80]</sup> The core electrons and their interaction with the valence electrons were represented using projector augmented wave (PAW) pseudopotentials,<sup>[81]</sup> while the valence electrons were described using a plane-wave basis set with an optimal kinetic energy cutoff of 415 eV, as previously tested and validated.<sup>[21,38]</sup> The threshold for the electronic optimization was set at  $10^{-6}$  eV for the self-consistent field steps in all cases, and optimizations were considered converged when forces acting on atoms were below  $0.01 \text{ eV} \cdot \text{\AA}^{-1}$ . During the optimizations, all atomic positions and cell parameters were allowed to relax.

For all the studied cases,  $p(1 \times 1)$  hexagonal unit cells were used for modeling the structures, and optimal  $\Gamma$ -centred  $7 \times 7 \times 1$  Monkhorst-Pack<sup>[82]</sup>  $k$ -points grids were employed for the Brillouin zone integration, except for band structure calculations, explored along the  $\Gamma \rightarrow K \rightarrow M$  paths. The slab models were represented with 30 Å of vacuum perpendicular to the MXene 2D surface, since previous studies and present tests revealed to be enough to avoid interactions between repeated slabs,<sup>[39,83]</sup> and provided a good precision to the band alignment and vacuum energy calculations.<sup>[35]</sup>

To compare and validate the bandgap results obtained, the hybrid Heyd–Scuseria–Ernzerhof (HSE06)<sup>[84]</sup> functional and the GW<sup>[85]</sup> many-body perturbation theory method were employed for the promising cases harvested from the screening. While GW calculations are typically considered the gold standard for

accurate band gap predictions, they can be computationally expensive, and not feasible for the large number of cases studied in our research.<sup>[71]</sup> However, it is worth noting that PBE0 is known to provide bandgap values that are closer to GW results compared to other functionals, making it a suitable approach for the present study.<sup>[71]</sup>

Test calculations on structures optimized with PBE0 revealed that the geometry and density of states (DOS) were very similar to the ones obtained from PBE-relaxed geometries, and, given the higher computational cost of PBE0 structure optimizations, PBE0 single-point calculations were performed on PBE geometries, an approach successfully used in the past.<sup>[35]</sup> Nonetheless, PBE0 band structure calculations using plane waves still require high-computational resources, and, therefore, such calculations were carried out using the Fritz–Haber Institute ab initio materials simulation (FHI-AIMS)<sup>[86]</sup> package, which uses numerical atomic orbitals (NAOs) as a basis set, and explicitly includes all core electrons in the electronic structure calculations. Even though being an all-electron program, NAOs manage to use fewer basis functions than plane waves and thus outperform them when using hybrid functionals. The self-consistent field and optimization criteria for FHI-AIMS are set equivalent to the ones used in VASP, to maintain the same computational playground, and, hence, the same  $7 \times 7 \times 1$   $k$ -points grid and the  $\Gamma \rightarrow K \rightarrow M$  path was used for the band structure calculations. As a basis set, a light Tier-1 level was used, with a quality similar to Dunning Gaussian-type orbitals (GTO) aug-cc-pVDZ basis set.<sup>[87]</sup> To assess the dynamical stability of key promising MXenes cases, the phonon spectra were gained using PHONOPY,<sup>[88]</sup> obtained based on the force constants computed by density functional perturbation theory (DFPT) with VASP,<sup>[89]</sup> and employing to that end a  $p(4 \times 4)$  super-cell with a reduced  $3 \times 3 \times 1$   $k$ -points grid, and inspecting only the vibrational modes of the employed slab models.

## Acknowledgements

The authors acknowledge financial support from the Spanish *Ministerio de Ciencia e Innovación* through grants PID2021-126076NB-I00 and TED2021-129506B-C22, the unit of excellence *María de Maeztu* CEX2021-001202-M granted to the IQT-CUB, and the *Generalitat de Catalunya* 2021SGR00079 grant. Computational resources have been provided by the *Red Española de Supercomputación* (RES) QHS-2023-2-0017 and QHS-2023-3-0012 projects. Also, F.V. thanks the ICREA Academia Award 2023 Ref. Ac2216561.

## Conflict of Interest

The authors declare no conflict of interest.

## Data Availability Statement

The data that support the findings of this study are available from the corresponding author upon reasonable request.

## Supporting Information

Supporting Information is available from the Wiley Online Library or from the author.

## Keywords

Density Functional Theory, MXenes, Photocatalysis, Water Splitting

Received: February 21, 2024

Revised: April 25, 2024

Published online: April 27, 2024

- [1] J. Zhu, L. Hu, P. Zhao, L. Yoon, S. Lee, K. Y. Wong, *Chem. Rev.* **2020**, 120, 851.
- [2] B. Akarsu, M. Serdar Genç, *Fuel* **2022**, 324, 124465.
- [3] G. Squadruto, G. Maggio, A. Nicita, *Renew. Energy* **2023**, 216, 119041.
- [4] R. M. Navarro Yerga, M. C. Alvarez Galván, F. del Valle, J. A. Villoria de la Mano, J. L. G. Fierro, *ChemSusChem* **2009**, 2, 471.
- [5] Q. Weng, G. Li, X. Feng, K. Nielsch, D. Golberg, O. G. Schmidt, *Adv. Mater.* **2018**, 30, 1801600.
- [6] P. Kumbhakar, C. Chowde Gowda, C. S. Tiwary, *Front. Mater.* **2021**, 8, 721514.
- [7] X. Zhang, L. Hou, A. Ciesielski, P. Samorì, *Adv. Energy Mater.* **2016**, 6, 1600671.
- [8] M. Schleicher, M. Fyta, *ACS Appl. Electron. Mater.* **2020**, 2, 74.
- [9] C. He, C. Xu, W. Zhang, *ACS Appl. Mater. Interfaces* **2023**, 15, 57015.
- [10] W. Zhang, J. T. Hou, M. Bai, C. He, J. R. Wen, *Appl. Surf. Sci.* **2023**, 634, 157648.
- [11] G. Zhao, A. Wang, W. He, Y. Xing, X. Xu, *Adv. Mater. Interfaces* **2019**, 6, 1900062.
- [12] K. S. Novoselov, A. K. Geim, S. V. Morozov, D. Jiang, Y. Zhang, S. V. Dubonos, I. V. Grigorieva, A. A. Firsov, *Science* **2004**, 306, 666.
- [13] Y. Gogotsi, B. Anasori, *ACS Nano* **2019**, 13, 8491.
- [14] K. R. G. Lim, M. Shekhiriev, B. C. Wyatt, B. Anasori, Y. Gogotsi, Z. W. Seh, *Nat. Synth.* **2022**, 1, 601.
- [15] M. Naguib, O. Mashtalir, J. Carle, V. Presser, J. Lu, L. Hultman, Y. Gogotsi, M. W. Barsoum, *ACS Nano* **2012**, 6, 1322.
- [16] M. A. Hope, A. C. Forse, K. J. Griffith, M. R. Lukatskaya, M. Ghidui, Y. Gogotsi, C. P. Grey, *Phys. Chem. Chem. Phys.* **2016**, 18, 5099.
- [17] V. Kamysbayev, A. S. Filatov, H. Hu, X. Rui, F. Lagunas, D. Wang, R. F. Klie, D. Talapin, *Science* **2020**, 369, 979.
- [18] V. Natu, M. W. Barsoum, *J. Phys. Chem. C* **2023**, 127, 20197.
- [19] M. Naguib, M. Kurtoglu, V. Presser, J. Lu, J. Niu, M. Heon, L. Hultman, Y. Gogotsi, M. W. Barsoum, *Adv. Mater.* **2011**, 23, 4248.
- [20] K. Chaturvedi, V. Hada, S. Paul, B. Sarma, D. Malvi, M. Dhangar, H. Bajpai, A. Singhwale, A. K. Srivastava, S. Verma, *Top. Curr. Chem.* **2023**, 381, 11.
- [21] R. Morales-Salvador, J. D. Gouveia, Á. Morales-García, F. Viñes, J. R. B. Gomes, F. Illas, *ACS Catal.* **2021**, 11, 11248.
- [22] I. Persson, J. Halim, H. Lind, T. W. Hansen, J. B. Wagner, L. Å. Näslund, V. Darakchieva, J. Palisaitis, J. Rosen, P. O. Å. Persson, *Adv. Mater.* **2018**, 31, 1805472.
- [23] Z. W. Seh, K. D. Fredrickson, B. Anasori, J. Kibsgaard, A. L. Strickler, M. R. Lukatskaya, Y. Gogotsi, T. F. Jaramillo, A. Vojvodic, *ACS Energy Lett.* **2016**, 1, 589.
- [24] A. D. Handoko, K. H. Khoo, T. L. Tan, H. Jin, Z. W. Seh, *J. Mater. Chem. A* **2018**, 6, 21885.
- [25] M. R. Lukatskaya, O. Mashtalir, C. E. Ren, Y. Dall'Agnese, P. Rozier, P. L. Taberna, M. Naguib, P. Simon, M. W. Barsoum, Y. Gogotsi, *Science* **2013**, 341, 1502.
- [26] M. Karimipour, A. Paingott Parambil, K. Tabah Tanko, T. Zhang, F. Gao, M. Lira-Cantu, *Adv. Energy Mater.* **2023**, 13, 2301959.
- [27] M. Naguib, J. Halim, J. Lu, K. M. Cook, L. Hultman, Y. Gogotsi, M. W. Barsoum, *J. Am. Chem. Soc.* **2013**, 135, 15966.
- [28] L. Chen, X. Dai, W. Feng, Y. Chen, *Acc. Mater. Res.* **2022**, 3, 785.
- [29] Q. Zhong, Y. Li, G. Zhang, *Chem. Eng. J.* **2021**, 409, 128099.
- [30] H. Zhang, M. Li, J. Cao, Q. Tang, P. Kang, C. Zhu, M. Ma, *Ceram. Int.* **2018**, 44, 19958.
- [31] Y. Li, X. Deng, J. Tian, Z. Liang, H. Cui, *Appl. Mater. Today* **2018**, 13, 217.
- [32] X. Li, J. Liu, G. Jiang, X. Lin, J. Wang, Z. Li, *J. Colloid Interface Sci.* **2023**, 643, 174.
- [33] X. Zhang, Z. Zhang, J. Li, X. Zhao, D. Wu, Z. Zhou, *J. Mater. Chem. A* **2017**, 5, 12899.
- [34] Z. Guo, J. Zhou, L. Zhu, Z. Sun, *J. Mater. Chem. A* **2016**, 4, 11446.
- [35] D. Ontiveros, F. Viñes, C. Sousa, *J. Mater. Chem. A* **2023**, 11, 13754.
- [36] I. Ibrahim, S. Abdel-Azeim, A. El-Nahas, O. Kühn, C. Chung, A. El-Zatahry, M. Shibl, *J. Phys. Chem. C* **2022**, 126, 14886.
- [37] Y. Sun, D. Jin, Y. Sun, X. Meng, Y. Gao, Y. Dall'Agnese, G. Cheng, X. Wang, *J. Mater. Chem. A* **2018**, 6, 9124.
- [38] J. D. Gouveia, F. Viñes, F. Illas, J. R. B. Gomes, *Phys. Rev. Mater.* **2020**, 4, 54003.
- [39] A. Jurado, Á. Morales-García, F. Viñes, F. Illas, *J. Phys. Chem. C* **2021**, 125, 26808.
- [40] V. Wang, G. Tang, Y. Liu, R. Wang, H. Mizuseki, Y. Kawazoe, J. Nara, W. Geng, *J. Phys. Chem. Lett.* **2022**, 13, 11581.
- [41] S. Guha, A. Kabiraj, S. Mahapatra, *NPJ Comput. Mater.* **2022**, 8, 202.
- [42] J. Yan, D. Cao, M. Li, Q. Luo, X. Chen, L. Su, H. Shu, *Small* **2023**, 19, 2303675.
- [43] N. Shah, X. Wang, J. Tian, *Mater. Chem. Front.* **2023**, 7, 4181.
- [44] J. Peng, X. Chen, W.-J. Ong, X. Zhao, N. Li, *Chem* **2019**, 5, 18.
- [45] Á. Morales-García, F. Viñes, C. Sousa, F. Illas, *J. Phys. Chem. Lett.* **2023**, 14, 3712.
- [46] F. Viñes, M. Bernechea, G. Konstantatos, F. Illas, *Phys. Rev. B* **2016**, 94, 235203.
- [47] A. Iglesias-Juez, F. Viñes, O. Lamiel-García, M. Fernández-García, F. Illas, *J. Mater. Chem.* **2015**, 3, 8782.
- [48] A. Migani, L. Blancafort, *J. Am. Chem. Soc.* **2016**, 138, 16165.
- [49] A. Migani, L. Blancafort, *J. Am. Chem. Soc.* **2017**, 139, 11845.
- [50] A. Fujishima, K. Honda, *Nature* **1972**, 238, 37.
- [51] A. Wolcott, W. A. Smith, T. R. Kuykendall, Y. Zhao, J. Z. Zhang, *Adv. Funct. Mater.* **2009**, 19, 1849.
- [52] Z. Guo, F. Ambrosio, A. Pasquarello, *ACS Catal.* **2010**, 10, 13186.
- [53] M. Khazaei, M. Arai, T. Sasaki, C.-Y. Chung, N. S. Venkataramanan, M. Estili, Y. Sakka, Y. Kawazoe, *Adv. Funct. Mater.* **2013**, 23, 2185.
- [54] X. Hai, J. Tahir-Kheli, W. A. Goddard, *J. Phys. Chem. Lett.* **2011**, 2, 212.
- [55] A. Champagne, J. C. Charlier, *J. Phys. Mater.* **2020**, 3, 32006.
- [56] M. Khazaei, A. Ranjbar, M. Arai, T. Sasaki, S. Yunoki, *J. Mater. Chem. C* **2017**, 5, 2488.
- [57] S. Ma, X. Fan, Y. An, D. Yang, Z. Luo, Y. Hu, N. Guo, *J. Mater. Sci.* **2019**, 54, 11378.
- [58] T. Hu, Z. Li, M. Hu, J. Wang, Q. Hu, Q. Li, X. Wang, *J. Phys. Chem. C* **2017**, 121, 19254.
- [59] S. Trasatti, *Pure Appl. Chem.* **1986**, 58, 955.
- [60] M. Khazaei, M. Arai, T. Sasaki, A. Ranjbar, Y. Liang, S. Yunoki, *Phys. Rev. B* **2015**, 92, 75411.
- [61] L. Zhou, Y. Zhang, Z. Zhuo, A. J. Neukirch, S. Tretiak, *J. Phys. Chem. Lett.* **2018**, 9, 6915.
- [62] A. Mostafaei, M. Abbasnejad, *J. Alloys Compd.* **2021**, 857, 157982.
- [63] S. Y. Zhang, N. P. Shi, C. K. Wang, G. P. Zhang, *Phys. Chem. Chem. Phys.* **2024**, 26, 412.
- [64] Q. Chen, D. Zhang, J. Pan, W. Fan, *Optik* **2020**, 219, 165046.
- [65] R. Meshkian, Q. Tao, M. Dahlqvist, J. Lu, L. Hultman, J. Rosen, *Acta Mater.* **2017**, 125, 476.
- [66] Y. Li, Y. Qin, K. Chen, L. Chen, X. Zhang, H. Ding, M. Li, Y. Zhang, S. Du, Z. Chai, Q. Huang, *J. Inorg. Mater.* **2021**, 36, 773.
- [67] J. Lu, A. Thore, R. Meshkian, Q. Tao, L. Hultman, J. Rosen, *Cryst. Growth Des.* **2017**, 17, 5704.
- [68] Y. Jiang, Y. Zhang, Q. Huang, L. Hao, S. Du, *J. Mater. Res. Technol.* **2020**, 9, 14979.
- [69] K. Gaál-Nagy, *Phys. Rev. B* **2008**, 77, 24309.
- [70] J. Zhang, P. Zhou, J. Liu, J. Yu, *Phys. Chem. Chem. Phys.* **2014**, 16, 20382.
- [71] W. Chen, A. Pasquarello, *Phys. Rev. B* **2012**, 86, 35134.
- [72] Y. Wu, C. He, W. Zhang, *J. Am. Chem. Soc.* **2022**, 144, 9344.
- [73] N. Zhang, Y. Hong, S. Yazdanparast, M. A. Zaeem, *2D Mater.* **2018**, 5, 45004.
- [74] B. Akgenc, *Solid State Commun.* **2019**, 303, 113739.
- [75] P. Hohenberg, W. Kohn, *Phys. Rev.* **1964**, 136, 864.
- [76] W. Kohn, L. J. Sham, *Phys. Rev.* **1965**, 140, 1133.

- [77] G. Kresse, J. Hafner, *Phys. Rev. B* **1994**, 47, 558.
- [78] J. P. Perdew, K. Burke, M. Ernzerhof, *Phys. Rev. Lett.* **1996**, 77, 3865.
- [79] J. P. Perdew, W. Yue, *Phys. Rev. B* **1986**, 33, 8800.
- [80] C. Adamo, V. Barone, *J. Chem. Phys.* **1999**, 110, 6158.
- [81] P. E. Blöchl, *Phys. Rev. B* **1994**, 50, 17953.
- [82] H. J. Monkhorst, J. D. Pack, *Phys. Rev. B* **1976**, 13, 5188.
- [83] C. Ougherb, T. Ouahrani, M. Badawi, Á. Morales-García, *Phys. Chem. Chem. Phys.* **2022**, 24, 7243.
- [84] J. Heyd, G. E. Scuseria, M. Ernzerhof, *J. Chem. Phys.* **2003**, 118, 8207.
- [85] M. Hybersten, S. Louie, *Phys. Rev. B* **1986**, 34, 5390.
- [86] V. Blum, R. Gehrke, F. Hanke, P. Havu, V. Havu, X. Ren, K. Reuter, M. Scheffler, *Comput. Phys. Commun.* **2009**, 180, 2175.
- [87] F. Viñes, F. Illas, *J. Comput. Chem.* **2017**, 38, 523.
- [88] A. Togo, A. Tanaka, *Scr. Mater.* **2015**, DOI: [10.1016/j.scriptamat.2015.07.021](https://doi.org/10.1016/j.scriptamat.2015.07.021).
- [89] X. Gonze, C. Lee, *Phys. Rev. B* **1997**, 55, 10355.